International Journal of Geo-Information

MDPI

Article

Investigation of Post-Fire Debris Flows in Montecito

Yifei Cui [1], Deqiang Cheng [2,3,*] and Dave Chan [4]

1 Department of Civil and Environmental Engineering, Hong Kong University of Science and Technology, Clear Water Bay, Hong Kong, China; yifeicui@ust.hk
2 Key Laboratory of Mountain Hazards and Earth Surface Process, Institute of Mountain Hazards and Environment, Chinese Academy of Sciences, Chengdu 610041, China
3 University of Chinese Academy of Sciences, Beijing 100049, China
4 Department of Civil and Environmental Engineering, University of Alberta, Edmonton, AB T6G 2W2, Canada; dave.chan@ualberta.ca
* Correspondence: chengdq90@imde.ac.cn; Tel.: +86-16602806361

Received: 20 November 2018; Accepted: 20 December 2018; Published: 25 December 2018

Abstract: Debris flows in a burned area, post-fire debris flows, are considered as one of the most dangerous geo-hazards due to their high velocity, long run-out distance, and huge destruction to infrastructures. The rainfall threshold to trigger such hazards is often reduced compared with normal debris flow because ashes generated by mountain fires reduce the permeability of the top soil layer, thus increasing surface runoff. At the same time, burnt material and residual debris have very poor geo-mechanical characteristics, e.g., their internal friction angle and cohesion are typically low, and thus an intense rainfall can easily trigger some debris flows. Studying post-fire debris flow enables us to get a deeper understanding of disaster management. In this paper, the debris flow that occurred in Montecito, California, USA, and was affected by the Thomas Fire was used as a case study. Five major watersheds were extracted based on the digital elevation model (DEM). Remote sensing images were used to analyze the wildfire process, the extent of the burned areas, and the burn severity. The hypsometric integral (HI) and short-duration rainfall records of the watersheds around Montecito when the post-fire debris flows occurred were analyzed. Steep terrain, loose and abundant deposits, and sufficient water supply are the important conditions affecting the formation of debris flows. Taking watersheds as the research objects, HI was used to describe the geomorphic and topographic features, open-access rainfall data was used to represent the water supply, and burn severity represented the abundance of material sources. An occurrence probability model of post-fire debris flow based on HI, short-duration heavy rainfall, and burn severity was developed by using a logistic regression model in post-fire areas. By using this model, the occurrence probability of the post-fire debris flow in different watersheds around Montecito was analyzed based on the precipitation with time. Especially, the change characteristics of occurrence probability of debris flows over time based on the model bring a new perspective to observe the obvious change of the danger of post-fire debris flows and it is very useful for early warning of post-fire debris flows.

Keywords: post-fire debris flow; Montecito; hypsometric integral; logistic regression model; rainfall; Thomas Fire; mountain hazard

1. Introduction

Vegetation in the forest has the function of conserving water and preserving soil erosion. The branches and leaves of forest trees can greatly reduce the impact of rainwater on the surface of the earth. The spongy vegetation layer on the ground surface of wooded areas not only can dampen the impact of rainwater, but it can also absorb a large amount of water, thus reducing water infiltration into the ground. At the same time, a large number of interlaced forest roots can help to stabilize soil.

Forest fire is a common disaster in wooded areas, which poses a serious threat to the environment, life, and property [1,2]. Forest fire burns vegetation on hillsides, which enhances water infiltration into the ground and decreases the stability of slopes [3]. On the other hand, because there is no vegetation protection, the rate of water absorption by the soil may not exceed the rate of rainfall, and it could cause surface runoff. Cannon et al. [4] found that most post-fire debris flows are generated through the process of progressive entrainment of material eroded from hillslopes and channels. Post-fire debris flows are initiated by runoff and erosion, rather than shallow landslides [5], and they can grow in size through erosion and scour during the movement [6]. When a large amount of ash layer and loose sediment appear as rich material sources after mountain fires, the process of progressive entrainment may become easier. As a result, the threshold of rainfall to induce debris flows is reduced obviously. Short et al. [7] conducted research about a post-fire debris flow in western Montana, and they found that the probability of debris flows increased by 50% after forest fires. Debris flow often damages highway, railway, and other transportation facilities, even villages and towns, causing huge losses [8–13].

Compared with traditional debris flow, some important parameters related to post-fire debris flow should be taken into consideration when modifications of the conventional debris flow prediction method are made. Currently, the prediction of post-fire debris flow mainly focuses on occurrence probability, frequency, and scale. Cannon et al. [14,15] studied the peak flow prediction of post-fire debris flows using the basin gradient, burn extent, and storm rainfall. Gartner et al. [16] also used variables, including basin areas burned at different severities, measures of basin morphology, rock type, soil material properties, rainfall amounts, and intensities for storms, to construct empirical models to predict the volumes of debris flows. Cannon et al. [17] used areal burned extent, soil properties, basin morphology, and rainfall from short-duration and low-recurrence-interval convective rainstorms to construct models to describe post-fire debris-flow probability. Gartner et al. [18] proposed a prediction function of erosion probability for post-fire debris flows based on channel slope, plane curvature, and channel length by conducting a comparison among factors, including contributing drainage basin area, channel slope, planform curvature, burn severity, and the upstream channel length, resulting in good accuracy and precision. It could be stated that different researchers use various evaluation factors. Based on the data-driven theory and genetic programming algorithm, Friedel [19] considered that the nonlinear equation established by three indexes, the average slope of the basin, the total burned area, and the total rainfall, has the least prediction error for the debris-flow scale. If only rainfall factors are used, it is also a common method to judge the occurrence probability of post-fire debris flows by rainfall intensity–duration thresholds [4,20].

The above research shows that it is feasible to construct forecast models to study the occurrence probability of post-fire debris flow. Complicated parameters in models would increase the uncertainty [21] and difficulty of the model application. Therefore, using a reduced number of key factors, like Friedel [19], may be easier to establish forecast models of watersheds affected by wide fire. Steep terrain, loose and abundant deposits, and sufficient water supply are the important conditions affecting the formation of debris flows. Currently, the geomorphic and topographic characteristics of debris flow can be better reflected by hypsometric integral (HI) [22] based on watershed units. Burn severity calculated from remote sensing images could represent the abundance of material sources. An important effect of mountain fires is the change of the rainfall threshold for hazards occurring due to the amount of ash produced by mountain fires. Different from the effect of long-time antecedent rainfall for ordinary debris flow, short-duration rainfall plays an important role in the occurrence of post-fire debris flows [23]. In this paper, HI, burn severity, and short-duration rainfall characteristics of the watersheds around Montecito were analyzed firstly. After that, these three factors were selected to conduct the logistic regression model of occurrence probability of the debris flows in post-fire areas. The change of post-fire debris flow occurrence probability around Montecito was then analyzed from the newly proposed model based on different rainfall in different periods.

2. Background and Study Area

Montecito is an unincorporated community and census-designated place in Santa Barbara County, California, located east of the City of Santa Barbara. Located at the foot of the Santa Ynez Mountains, which are young and mostly of sedimentary origin, the peak elevation around Montecito has an altitude of 981 m. Montecito experiences a cool Mediterranean climate characteristic with warmer winters and cooler summers compared with places further inland because of Montecito's proximity to the ocean.

Early on the morning of 9 January 2018, about one month since the start of Thomas Fire, a heavy rainfall caused mud and boulders from the Santa Ynez Mountains to flow down creeks and valleys into Montecito [24] (Figure 1). This post-fire debris flows consisting of mud, boulders, and tree branches were up to 15 feet (5 m) in height, moving at estimated speeds of up to 20 miles per hour (30 km/h) into the lower areas of Montecito [25]. The cascading processes resulted in 21 deaths and two missing persons [26]. About 163 people were hospitalized for various injuries [27]. The disaster caused at least $177 millions of property damage, at least $7 millions in emergency responses, and another $43 millions in cleaning costs [28,29].

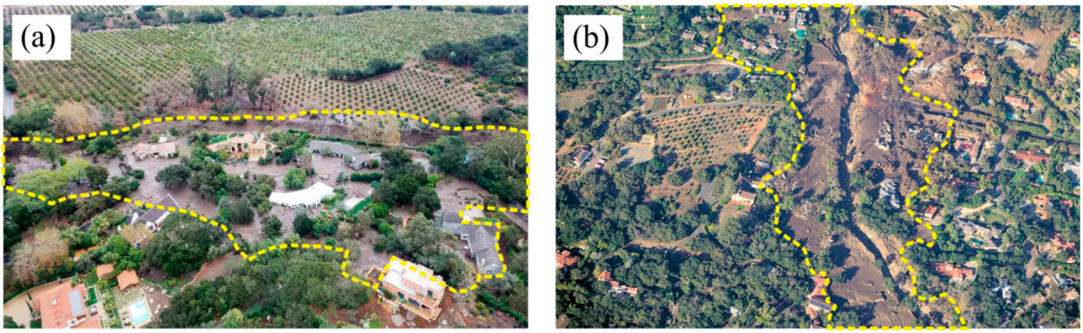

Figure 1. Disaster photos in which the areas affected by the debris flows are circled with yellow lines. (**a**) Homes and streets of a neighborhood affected by the Santa Barbara County mudslides in Santa Barbara, California on 9 January 2018, from the perspective of a Coast Guard MH-65 Dolphin helicopter crew involved in rescuing injured and stranded victims. (Modified from U.S. Coast Guard photo [30]); (**b**) San Ysidro Ranch and Casa de Maria damage taken on 11 January 2018 due to the catastrophic debris flow from heavy rains after the Thomas Fire, modified from [31].

The post-disaster high-resolution remote sensing image of WorldView-2 on 13 January 2018 was downloaded from Google Earth. By using image interpretation of the post-disaster remote sensing image, it was found that debris flows affecting Montecito mainly broke out in five watersheds (Figure 2). The impact areas of these post-fire debris flows are different, among which the debris flows coming from the first and third basins caused huge damage to downstream residential areas (Table 1). Mass mud came out of the mountain passes and rushed into the city to form a number of debris-flow accumulation areas with different thicknesses of mud.

Table 1. Watershed area and accumulation area of different debris flows.

Watershed Number	Watershed Area (km^2)	Accumulation Area (km^2)
①	9.35	0.78
②	1.47	0.08
③	7.60	0.69
④	1.67	0.11
⑤	4.59	0.17

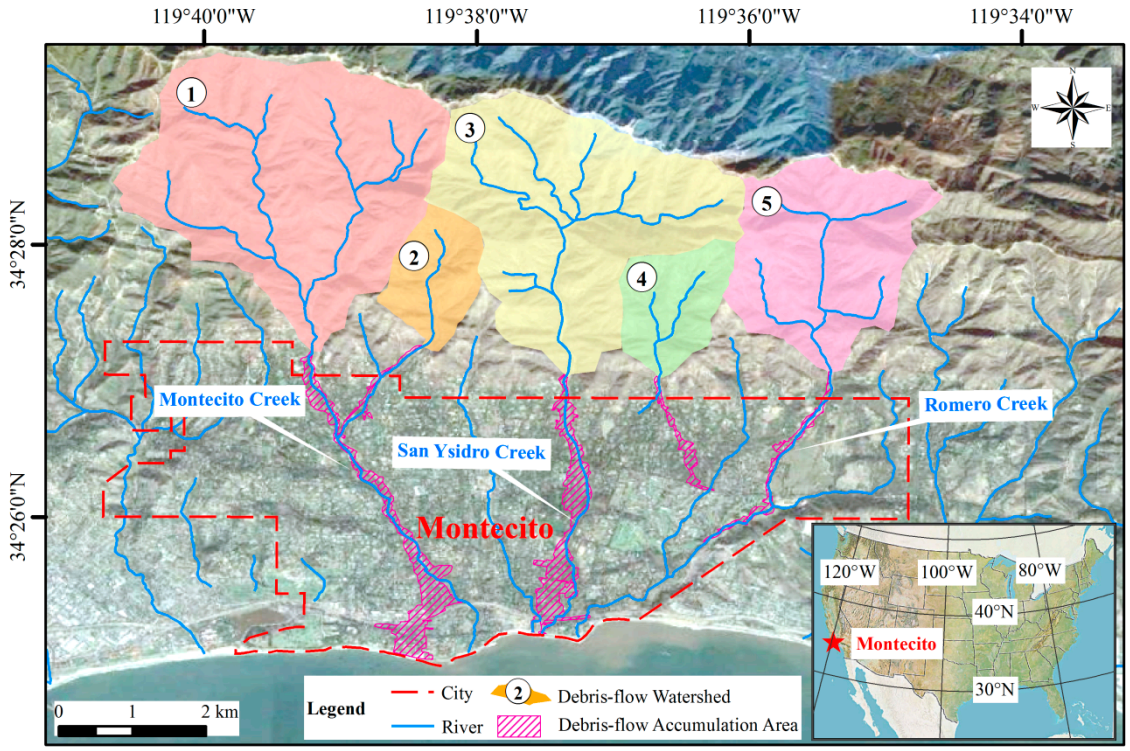

Figure 2. Debris-flow watersheds and debris-flow accumulation area around Montecito.

3. Materials and Methods

3.1. Materials

Free remote sensing data are easy to obtain through the internet, such as Landsat satellite images [32,33] of National Aeronautics and Space Administration (NASA) which can be downloaded from the United States Geological Survey (USGS) Global Visualization Viewer (GloVis) website (https://glovis.usgs.gov/), and Sentinel satellite images [34,35] of European Space Agency (ESA), which can be downloaded from the Copernicus Open Access Hub website (https://scihub.copernicus.eu/dhus/#/home). These free satellite data can be used to analyze nature hazards - mountain fires [34], landslides [36], debris flow [37], and others. In this study, Landsat 8 data of 23 November 2017, Landsat 8 data of 9 December 2017, Sentinel-2A data of 13 December 2017, Landsat 7 data of 17 December 2017, Landsat 8 data of 25 December 2017, Sentinel-2A data of 12 January 2018, and Landsat 8 data of 26 January 2018 were downloaded to analyse the fire. The Shuttle Radar Topography Mission (SRTM) Digital Elevation Model (DEM) data with a 30-m resolution from United States Geological Survey (USGS) was used for watershed extraction. Rainfall data were obtained through the World Weather Online website [38].

3.2. Methods

3.2.1. Fire Analysis Using the Shortwave Infrared (SWIR) and Normalized Burn Ratio (NBR)

Shortwave infrared (SWIR) can penetrate haze and smoke, so SWIR images can be used to identify and analyze active forest fire [39,40]. Taking Landsat 8 data as an example, the fire smoke can be seen in the true color image (Figure 3a). However, it is difficult to identify the burned areas. In the false-color composite image of shortwave infrared data (R = SWIR2, G = SWIR1, and B = SWIR2), the burned areas are revealed as pink color (Figure 3b).

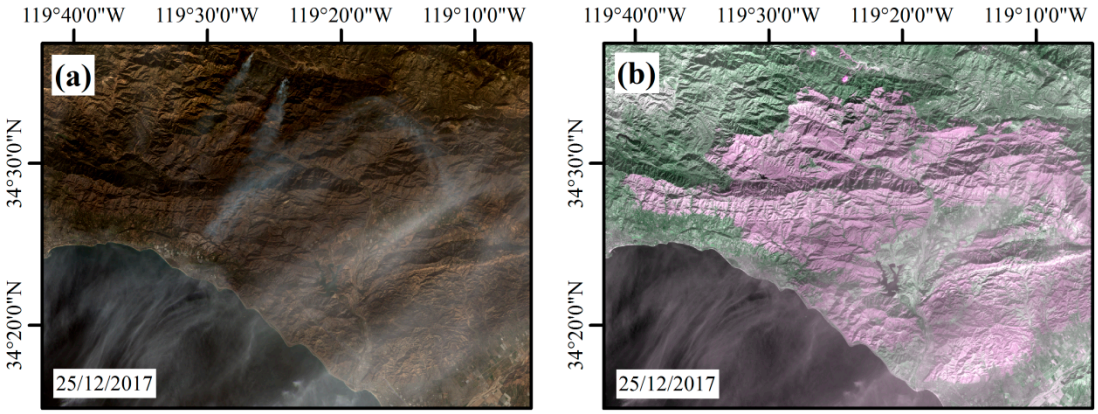

Figure 3. Fire analysis using Shortwave Infrared (SWIR). (**a**) True color image; (**b**) false color image (R = SWIR2, G = SWIR1, and B = SWIR2).

A normalized burn ratio (NBR) is defined to index the severity of a burn using multispectral remote sensing images. The formula for NBR uses the near-infrared band and the short-wave infrared band [41,42]:

$$NBR = \frac{NIR - SWIR}{NIR + SWIR} \quad (1)$$

where *NIR* is the near-infrared band and *SWIR* is the short-wave infrared band. *NIR* and *SWIR* can be reflectance, radiance, or digital number (DN) as measured in bands 4 (0.76–0.90 µm) and 7 (2.08–2.35 µm) of the Thematic Mapper (TM) images, in bands 4 (0.775–0.90 µm) and 7 (2.09–2.35 µm) of the Enhanced Thematic Mapper Plus (ETM+) images, or in bands 5 (0.845–0.885 µm) and 7 (2.10–2.30 µm) of the Operational Land Imager (OLI) images.

For a burned area, NBR_b is calculated before the burn and NBR_p is calculated from an image immediately following the burn. Burn severity is calculated by taking the difference between these two index layers [43]:

$$\Delta NBR = NBR_b - NBR_p \quad (2)$$

Table 2 from the USGS FireMon program can be used as a first approximate for interpretation of *NBR* differences corresponding to different burn severity [44].

Table 2. Burn severity categories.

ΔNBR	Burn Severity
<−0.25	High post-fire regrowth
−0.25 to −0.1	Low post-fire regrowth
−0.1 to +0.1	Unburned
0.1 to 0.27	Low-severity burn
0.27 to 0.44	Moderate-low severity burn
0.44 to 0.66	Moderate-high severity burn
>0.66	High-severity burn

3.2.2. Watershed Extraction Method Based on 30-m Resolution Shuttle Radar Topography Mission (SRTM) Digital Elevation Model (DEM) Data

A watershed is a hydrological unit commonly used in natural resource management and planning. It is more common to study debris flow hazards based on watershed units [45–47]. In this paper, the extraction of watersheds by creating a watershed boundary was achieved using 30-m resolution Shuttle Radar Topography Mission (SRTM) Digital Elevation Model (DEM) data in ArcGIS software. A sink is a cell or set of spatially connected cells, which are surrounded by higher value grids. Sink filling is the first step for the extraction of the basin boundary. It can help to remove small imperfections in the data by adding the pixel value to the lowest pixel value around it [48]. Grids whose sinks are

filled can be used to obtain the drainage direction of each grid. The widely used method of determining the flow direction is the eight-direction method, which makes the direction of a pixel to point to a lower pixel, which has the maximum gradient in the surrounding eight pixels [49]. Based on the flow-direction grids, the flow-accumulation grids list the number of pixels flowing through it for each pixel. Using the conditional function to set a threshold of the flow-accumulation grids, drainage networks could be obtained. Pour points at the outlet of each watershed were drawn. Using the ArcGIS "watershed" tool, in which the flow-direction raster and pour-point data were used as input data, the contributing areas above different pour points in a raster data were determined as ranges of watersheds.

3.2.3. Hypsometric Integral

The hypsometric integral (HI) is a quantitative index to study the relationship between the horizontal section area and its elevation in a watershed. HI reflects the landform erosion stage and evolution process. Strahler [50] divided geomorphic development into three stages—young stage (HI $\geq$ 0.60), mature stage (0.35 < HI < 0.60), and old stage (HI $\leq$ 0.35). When calculating an HI value, contour i is chosen as a reference, the whole watershed area is A, and the area above the contour of the basin is a_i. The height difference between the contour and the lowest point of the basin is h_i, and the height difference between the highest and lowest points is H. The variables are set as:

$$x_i = \frac{a_i}{A}, \tag{3}$$

$$y_i = \frac{h_i}{H}, \tag{4}$$

where x_i is the area percentage based on contour i, and y_i is the percentage of relative height difference. The points (x_i, y_i) in the rectangular coordinate system are spread to form a curve. It can be defined as:

$$y = f(x), \tag{5}$$

On this basis, the HI value is calculated by a definite integral value in the range of 0 to 1 in Equation (6) by using integral curve method:

$$\mathrm{HI} = \int_0^1 f(x)dx, \tag{6}$$

Formula (6) belongs to the integral curve method. Pike and Wilson [51] proposed the elevation-relief ratio method by deducing a mathematical formula to estimate the HI value. It can be defined as:

$$\mathrm{HI} \approx \frac{H_{ave} - H_{min}}{H_{max} - H_{min}} \tag{7}$$

where H_{ave} is the average elevation value of a watershed, H_{min} is the minimum elevation value of a watershed, and H_{max} is the maximal elevation value of a watershed.

By comparing the above methods, Chang et al. [52] found that the HI values calculated by the methods are almost the same. However, the method of the elevation-relief ratio is more efficient and simpler to calculate the HI value. Therefore, the elevation-relief ratio method used in Equation (7) was chosen in this study.

3.2.4. Logistic Regression Model

Although there are many advanced techniques and methods, such as the neural network method [53], conditional probability, and support vector machine [54,55], used in developing a susceptibility mapping of natural hazards, the logistic regression model, as a widespread methodology with the advantage of being simple and easy to implement [55–59], was used in this study to develop

the occurrence probability model of post-fire debris flows. Logistic regression (LR) is a regression model in which the dependent variable (DV) is categorical. The output can take only two values, "0" and "1", which represent outcomes, such as win/lose, alive/dead, or healthy/sick [60]. Logistic regression is an example of a qualitative response model. In this study, the relationship between the probability of the occurrence of post-fire debris flow and the influencing factors can be expressed as [61]:

$$Z = B_0 + B_1X_1 + B_2X_2 + \ldots + B_nX_n, \tag{8}$$

$$P = \frac{1}{1 + e^{-Z}}, \tag{9}$$

In this study on the occurrence probability of post-fire debris flow, P represents the probability, and the output result ranges from 0 to 1. Z is the sum of linear weights after superposition of variables, and Bi is a regression coefficient.

3.2.5. Technical Route

The methods used in this paper are described above. In order to make the structure of the article clearer, the technical route is made (Figure 4). In this study, we attempted to take the post-fire debris flow that occurred in Montecito, California, USA as a case study to develop the occurrence probability of post-fire debris flows using several important influencing factors. Firstly, three factors affecting post-fire debris flow in five basins around Montecito were analyzed. We then selected a wider range of data in a larger area covering Montecito to build the logistic regression model in order to enhance the robustness of the model. The model was applied to the five watersheds around Montecito to find the change of occurrence possibility of post-fire debris flow along with rainfalls at different times.

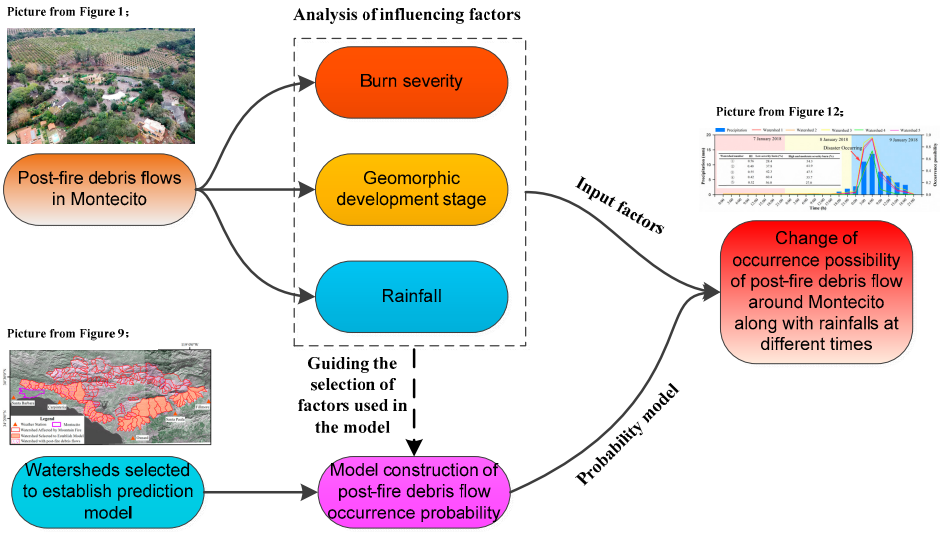

Figure 4. Technical route of this study.

4. Data Interpretation and Model Construction

4.1. Data Interpretation

4.1.1. The Spread of Mountain Fires and Burn Severity around Montecito

Landsat 8 data on 9 December 2017 (Figure 5a), Sentinel 2A data on 13 December 2017 (Figure 5b), Landsat 7 data on 17 December 2017 (Figure 5c), and Landsat 8 data on 25 December 2017 (Figure 5d) were selected to get the burned area using SWIR false color composite images in which burned areas are displayed with pink color. According to the contrast of multi-temporal images, the Thomas Fire, which began on 4 December, had not affected Montecito until 9 December 2018. While on

13 December 2017, mountain fires were burning fiercely, and the range of fires in this area no longer expanded on 17 December 2017, which is more than 20 days from 9 January 2018 when the disaster occurred.

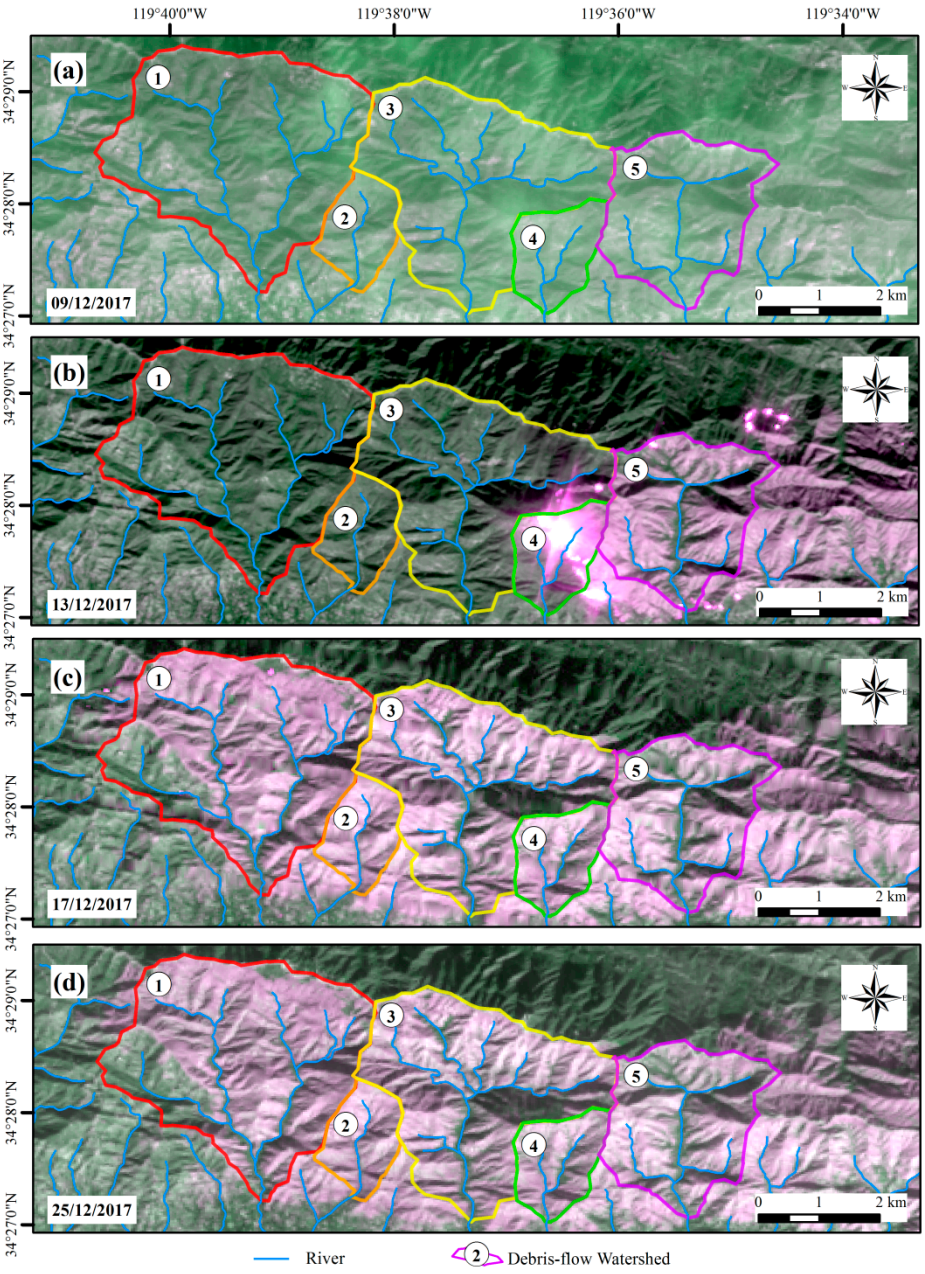

Figure 5. Fire process around Montecito area analyzed by remote sensing images of: (**a**) 9 December 2017; (**b**) 13 December 2017; (**c**) 17 December 2017; (**d**) 25 December 2017.

The Landsat 8 images on 23 November 2017 and on 26 January 2018 were used to calculate the normalized burn ratio (NBR) separately as the pre-fire NBR and post-fire NBR. Burn severity was calculated by taking the difference between the above two indexes (Figure 6). It can be found that most of the watersheds were moderate burn that could provide a great deal of loose source for debris flow.

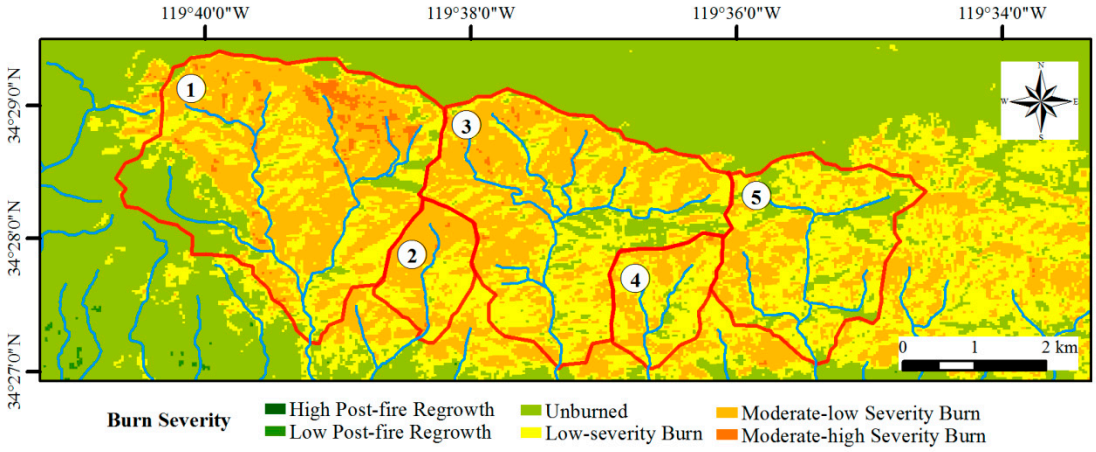

Figure 6. Burn severity around Montecito.

4.1.2. Geomorphic Development Stage

Using DEM data downloaded from the USGS website [62] and the HI calculation method, the hypsometric integral curves of the different watersheds around Montecito were drawn, as shown in Figure 7, and HI values of them were calculated. According to the HI-based geomorphic development stages proposed by Strahler, and the summary of watershed hypsometric integral curves [22,63], the geomorphic development in Figure 7 is divided into three stages. The area above the convex curve is considered as the young stage; the area below the concave curve is treated as the old stage; the area between the two curves is known as the mature stage [8]. According to Figure 7, the five watersheds around Montecito belong to the mature stage. In the infancy and mature periods, the terrain was steep and the solid content of the gully was rich. Therefore, mature stage watersheds have a susceptible geomorphic environment for debris flows.

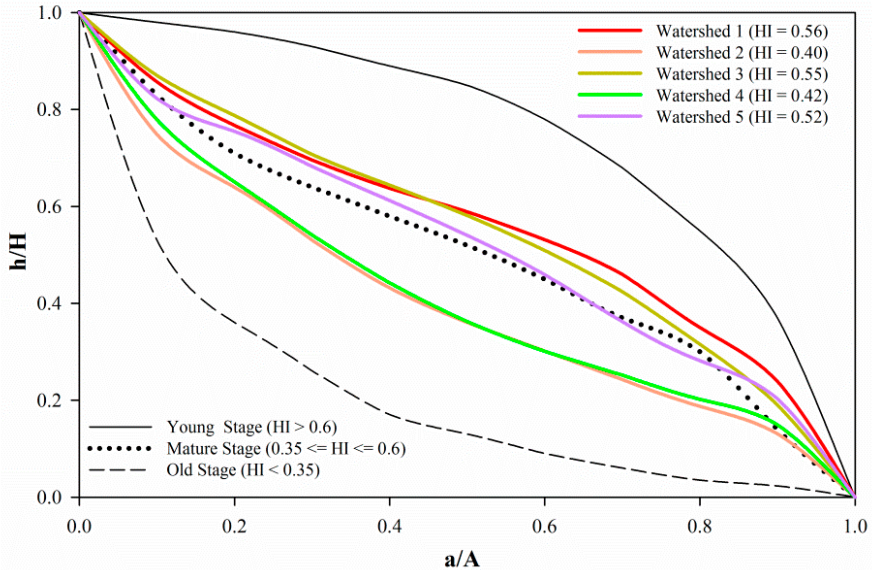

Figure 7. Hypsometric integral curve. The black line represents the three stages of the development of the watershed geomorphology.

4.1.3. Rainfall

Post-fire debris flows generally are triggered by one of two processes: Surface erosion caused by rainfall-induced runoff, and slope failure caused by rainfall infiltration. Runoff-dominated processes are by far the most prevalent because fires commonly reduce the infiltration capacity of soils, which increases runoff and erosion [64]. Rainfall conditions are often regarded as the triggering

factor of post-fire debris flows. The influence of mountain fire makes the threshold of rainfall decrease obviously compared with ordinary debris flow. The debris can begin to slide after a rain of 8 mm with a time interval of only 30 min [23]. In the current study, Montecito's local rainfall data of a three-hour interval were obtained through the World Weather Online website [38]. The first measurable rain for the area around Montecito fell on 8 January 2018. Ash and loose sediment generated by forest fires formed the source of debris flow development. A heavy rainfall process occurred at about 3:00 on the morning of 9 January 2018 (Figure 8a), causing mud and boulders from the gullies to flow along several drainage basins into Montecito. The comparison of rainfall data during the same period in 2018 with 2017 is shown in Figure 8. It is observed that no debris flow occurred on 9 January 2017, with a cumulative precipitation of 16.5 mm (Figure 8b), while the debris flow occurred on 9 January 2018, with a cumulative precipitation of less 13.7 mm (Figure 8a). It can be seen that the rainfall threshold of debris flows in the burned area decreased obviously after the Thomas Fire.

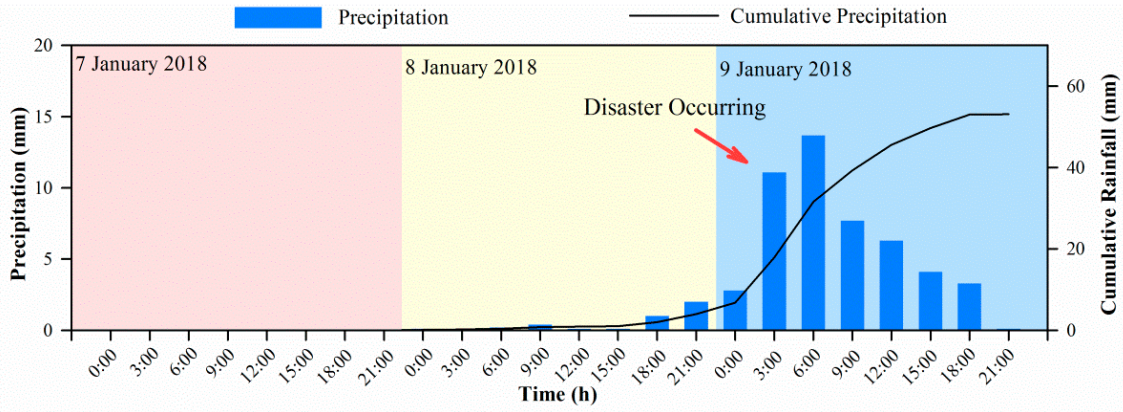

(**a**)

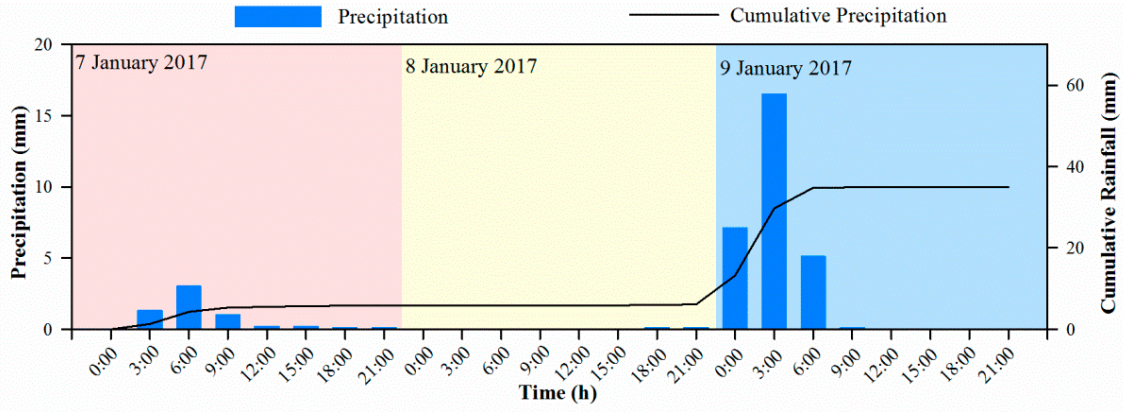

(**b**)

Figure 8. Rainfall in Montecito during the period from (**a**) 7 January to 8 January 2018 with a cumulative precipitation of less 13.7 mm; (**b**) 7 January to 8 January 2017 with a cumulative precipitation of 16.5 mm [38].

4.2. Model Construction of Post-Fire Debris Flow Occurrence Probability

In the current study, burn severity, HI, and short-duration rainfall in the Montecito post-fire debris flow disaster were discussed to illustrate their relationships with post-fire debris flows. To build a good model between them, we needed more data to support it. The watersheds affected by the Thomas Fire were detected using an SWIR false-color image of Sentinel-2A data on 12 January 2018 (Figure 9). Firstly, 380 rainfall records of 63 watersheds at different times were obtained. Remote sensing images of Google Earth at different times after the Thomas Fire were used to determine whether or not the

post-fire debris flows occurred. We took the scouring and accumulation characteristic of debris flows at the outlet of the main river course as the criterion for the occurrence of debris flow. Debris flows that did not produce significant deposits at the basin outlet were not included. 1 and 0 were used to express the occurrence and non-occurrence and were input into the logistic regression model. As shown in the figure below, 30 of the watersheds used to construct the model can be identified traces of debris flows in the main channel.

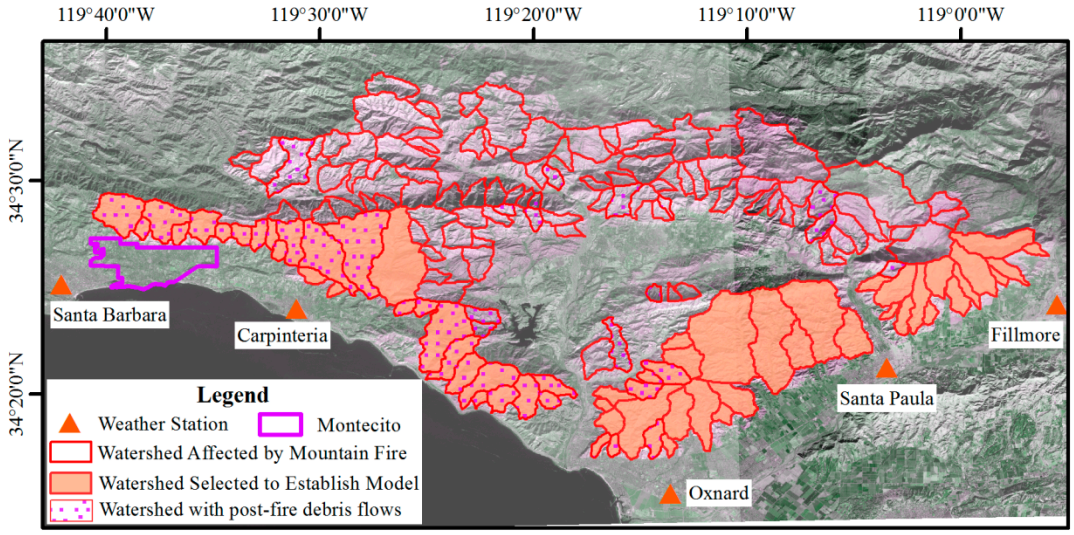

Figure 9. Watersheds selected to establish the prediction model to analyze the occurrence probability of post-fire debris flows.

To construct a model between the debris flow occurring and the factors, including burn severity, HI, and short-duration (3-h interval) rainfall data, rainfall data were obtained through the World Weather Online website [38]. The burn severity image was calculated using the Landsat 8 data of 23 November 2017 and 26 January 2018 (Figure 10). The percentages of burn severity, including low-severity burn and high and moderate severity burn, of each watershed were calculated. The HI factors could also be calculated using DEM.

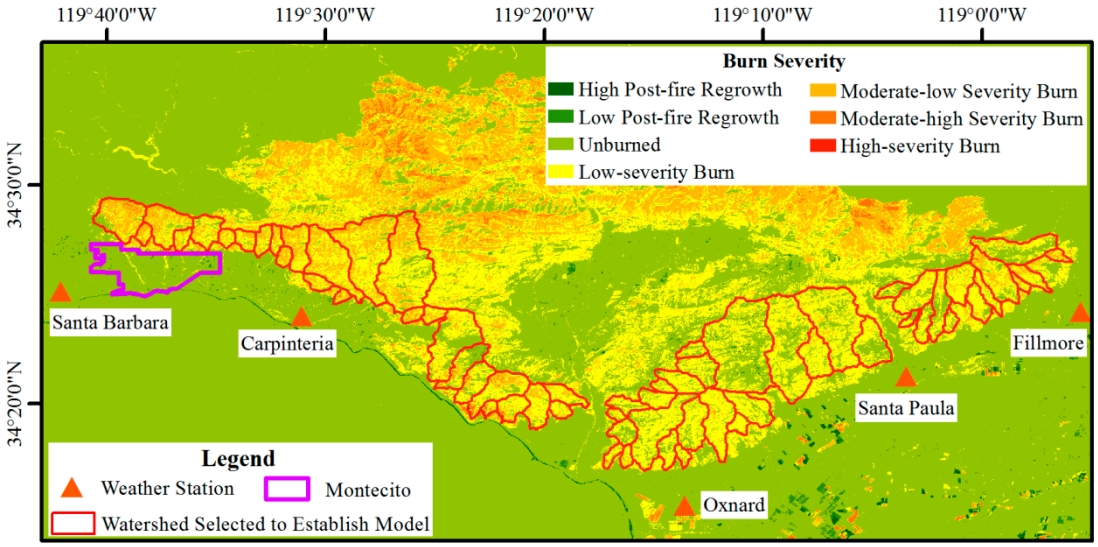

Figure 10. Burn severity affected by the Thomas Fire.

Taking the burn severity, HI, and rainfall as the independent variable, and the debris flow occurring as a dependent variable, by using the logistic regression model, the prediction model of the

post-fire debris flow occurrence probability was constructed according to Equation (9), as shown in Equation (11). The fitting parameter, R^2, of the model was 0.887, which indicates a good fitting degree.

$$Z = -22.563 + 20.263(HI) + 0.554(PR) + 8.6(\%Low\text{-}severity\ burn) + 7.404(\%High\ and\ moderate\ severity\ burn), \quad (10)$$

$$P = \frac{1}{1 + e^{-z}}, \quad (11)$$

In the above equations, P represents the probability of the occurrence of post-fire debris flows. Z is the sum of linear weights after superposition of variables. The probability of debris-flow occurrence (P) of an individual basin can be estimated as a function of:

- Hypsometric integral value of each basin (*HI*);
- total three-hour precipitation (*PR*, mm);
- percent of the low-severity burned area in each basin (*%Low-severity burn*); and
- percent of the high and moderate severity burned area in each basin (%Low-severity burn).

A receiver operating characteristic (ROC) curveis a graphical plot that illustrates the diagnostic ability of a binary classification system as its discrimination threshold is varied. The area under the curve is defined as the AUC (area under the curve, with a numeric range between 0.5 and 1). The classifier with a larger AUC value would be much better [65]. In this research, 22 new watersheds (Figure 11a), which were different from the ones for conducting the model, were used to generate the ROC curve. Using the "ROC curve" tool in the SPSS software, taking the P value calculated using the above model as the "Test Variable", the actual occurrence of the debris flow as the "State Variable" ("Value of State Variable" is 1), the ROC curve could be drawn, and the AUC value was calculated automatically (Figure 11b). Fressard et al. defined five classes of accuracy using the parameter, AUC: Excellent accuracy for AUC values from 0.9 to 1.0; good accuracy for AUC values from 0.8 to 0.9; fair accuracy for AUC values from 0.7 to 0.8; poor accuracy, for AUC values from 0.6 to 0.7; and fail accuracy, for AUC values from 0.5 to 0.6 [66]. In this paper, the AUC value was 0.876, which indicates a good accuracy of the prediction ability of the logistic regression model. We used 0.5 as the threshold of probability of the logistic regression model to judge the occurrence of debris flows. For the prediction of debris flow occurrence probability in the 22 watersheds, only one basin showed a negative result. The classification accuracy was 95%, which is a satisfactory result.

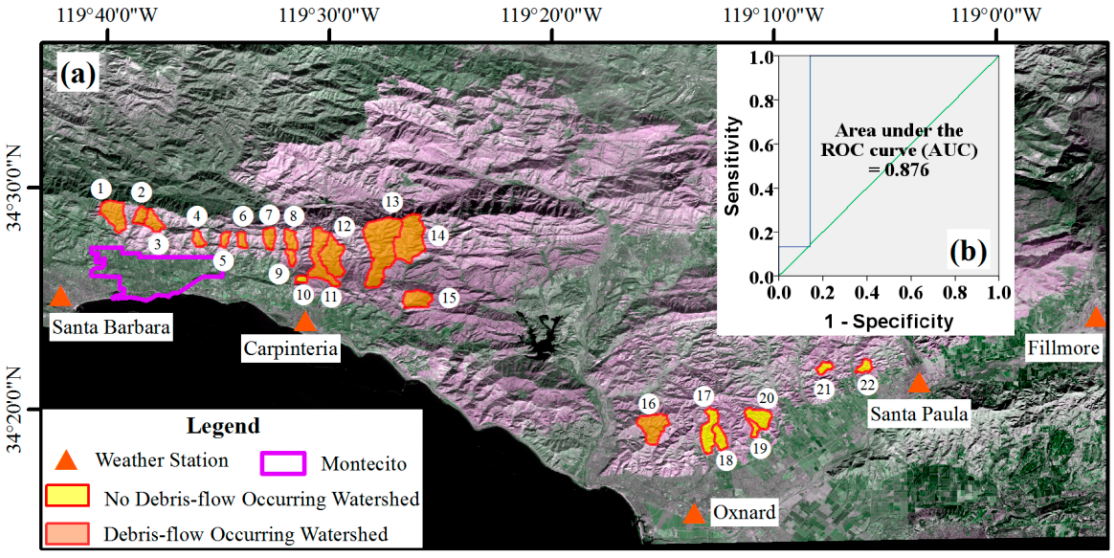

Figure 11. Model accuracy verification. (**a**) Watersheds used to be verified; (**b**) Receiver operating characteristic (ROC) curve and area under the curve (AUC) value.

5. Model Application around Montecito

The occurrence probabilities of post-fire debris flows in different watersheds around Montecito at a different time were calculated (Figures 12 and 13) by putting burn severity, HI, and rainfall into the model (Equations (10) and (11)). The probability change of post-fire debris flows due to the change of rainfall could reflect the danger change of post-fire debris flows in a long time.

The probability of debris flow occurrence in five watersheds varied differently with the rainfall process, as shown in Figures 12 and 13. It is observed that HI, short-duration heavy rainfall, and burn severity played different roles in this process.

(1) The occurrence probability of post-fire debris flow of watershed 1 increased first at the time of 21:00 on January 8. At the same time, the occurrence probability of post-fire debris flows of watershed 2 was lower than watershed 1, even with a higher burn severity. This may be attributed to a relatively lower HI value in watershed 2. A high value of HI indicates a steep terrain, which could enhance debris initiation. In these five watersheds, it was found that both watershed 2 and 4 also had a low probability of debris flow because of their small HI values.

(2) For a single basin, with the increase of rainfall, the probability of post-fire debris flow increased. All five basins had a peak of occurrence probability when the maximum rainfall occurred during the rainfall process. They faced the greatest threat when the rainfall reached its peak at 6:00 am on January 9 when rainfall played a dominant effect (Figure 12).

(3) The influence of the burn severity for the post-fire debris flows could be reflected by comparing watershed 1 with 3. The two watersheds experienced the same rainfall process and had similar HI values. However, watershed 3 was calculated with a higher probability of debris flow occurrence than watershed 1. This was mainly attributed to the different burn severity of the fire. According to Formula (10), it was found that the percent of the low-severity burned area and high and moderate severity burned area in each basin had a similar coefficient (8.6 compared with 7.4) in the equation. This means a similar effect when using them as the input to calculate the P value—the occurrence probability of post-fire debris flows. The reason why watershed 3 had a higher probability of debris flows was that it had a higher proportion of fire burn (89.8%) than watershed 1 (82.7%). A higher proportion of fire burn, including low-severity burn, high, and moderate severity burn, meant more material sources for the debris flows.

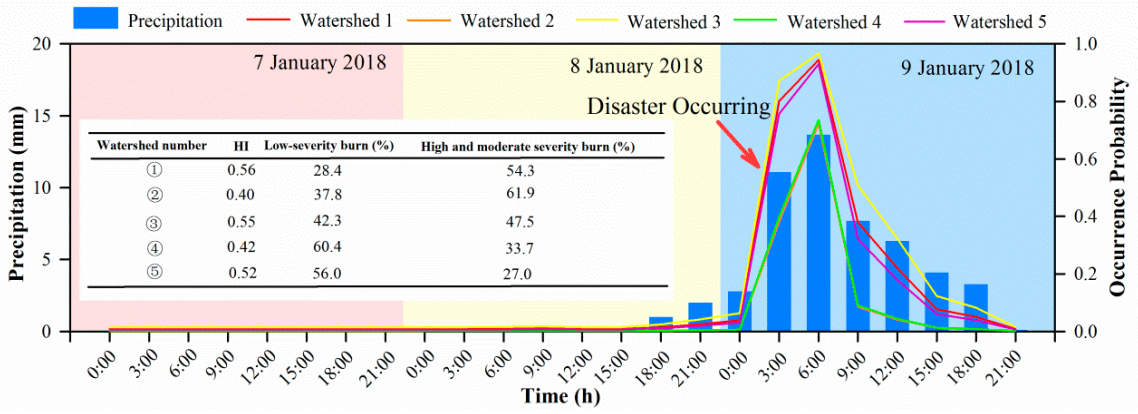

Figure 12. Change of post-fire debris flow occurrence probability of each watershed around Montecito along with rainfalls at different times.

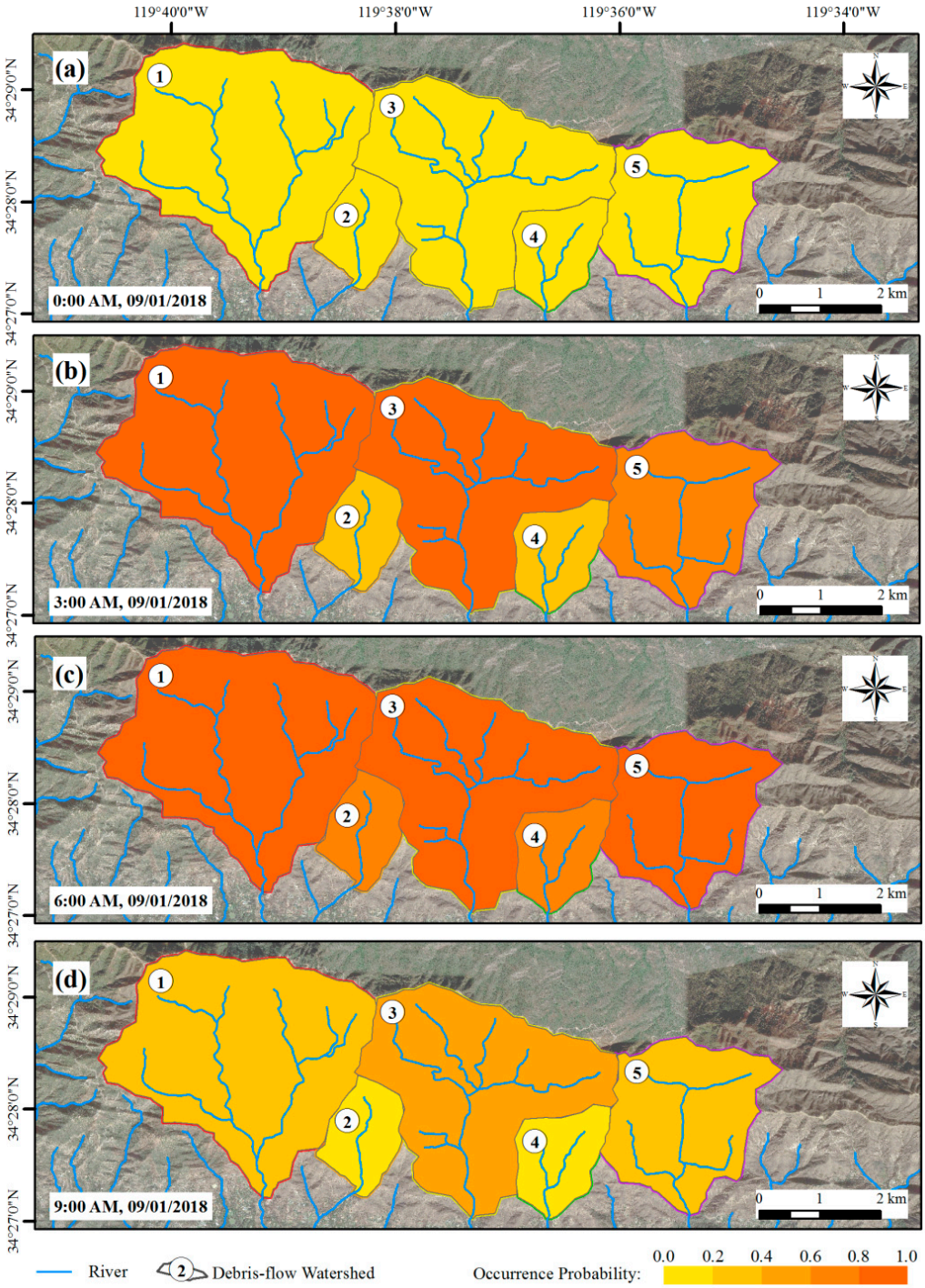

Figure 13. Spatial display of post-fire debris flow occurrence probability of each watershed around Montecito at different times on 9 January 2018: (**a**) 0:00 AM; (**b**) 3:00 AM; (**c**) 6:00 AM; (**d**) 9:00 AM.

6. Discussion and Conclusions

As a special type of geological disasters, post-fire debris flow is significantly different from an ordinary debris flow. In particular, the threshold of rainfall required for the occurrence of post-fire debris flows is reduced because mountain fires produce a large number of material sources. When studying the probability of post-fire debris flow by constructing a model, the factors selected by different scholars are different. Determining the key factors and reducing factor quantities are not only conducive to reducing uncertainty, but also can improve the accuracy of the forecast model for post-fire debris flow. The burn severity, HI, and rainfall factors selected in this paper play an important

role in the formation of post-fire debris flow. The characteristics of burn severity, HI, and rainfall factors in the post-fire debris flows of watersheds around Montecito were first analyzed. On a larger scale, 380 rainfall records corresponding to 380 events' records of 63 watersheds at different times were obtained, and a prediction model of post-fire debris flow was made by using a logistic regression model to represent the occurrence probability of debris flows in each watershed. The application of the model used for the five watersheds of Montecito had good results and also reflected the change of occurrence probability of post-fire debris flows around Montecito during a rainfall process. The change of occurrence probability due to changes in rainfall is very help for an early warning of post-fire debris flows.

On the other hand, one of the advantages of this model is that it is easy to use and practical. Input parameters are easy to obtain from the public source data. The HI value of each basin can be obtained before mountain fires. After the fire, the severity of the fire can be obtained by using remote sensing images quickly. Based on the weather forecast, the future rainfall can be known, and then by inputting the above variables into the model, the occurrence probability of future post-fire debris flows after fires can be obtained. It is helpful for disaster prevention and reduction. Nevertheless, the model is based on the mountain fire area in California, and the practicability of other regions needs further verification and the model parameters may need to be adjusted.

Author Contributions: Y.C. designed the method and conceived the study plan; D.C. performed the calculation and analyzed the data; Y.C., D.C., and D.C. wrote the paper.

Funding: This research was funded by the opening fund of the State Key Laboratory of Hydraulics and Mountain River Engineering (Grant No. SKHL1609). This research was also supported by the projects of the International partnership program of the Chinese Academy of Sciences (Grant No. 131551KYSB20160002), the Key Research Program of Frontier Sciences, CAS (Grant No. QYZDY-SSW-DQC006), and theme-based research grant provided by the Research Grants Council of Hong Kong (Grant No. T22-603/15-N).

Acknowledgments: The authors would like to thank all colleagues who participated in this study.

Conflicts of Interest: The authors declare no conflict of interest.

References

1. Jaiswal, R.K.; Mukherjee, S.; Raju, K.D.; Saxena, R. Forest fire risk zone mapping from satellite imagery and GIS. *Int. J. Appl. Earth Obs. Geoinf.* **2002**, *4*, 1–10. [CrossRef]
2. Siegert, F.; Ruecker, G.; Hinrichs, A.; Hoffmann, A.A. Increased damage from fires in logged forests during droughts caused by El Nino. *Nature* **2001**, *414*, 437. [CrossRef] [PubMed]
3. Mooney, H.A.; Bonnicksen, T.M.; Christensen, N.L.; Lotan, J.E.; Reiners, W.A. Proceedings of the conference fire regimes and ecosystem properties, December 11–15, 1978, Honolulu. *J. Chem. Eng. Data* **1981**, *37*, 470–473.
4. Cannon, S.H.; Gartner, J.E.; Wilson, R.C.; Bowers, J.C.; Laber, J.L. Storm rainfall conditions for floods and debris flows from recently burned areas in southwestern Colorado and southern California. *Geomorphology* **2008**, *96*, 250–269. [CrossRef]
5. Kean, J.W.; Staley, D.M.; Cannon, S.H. In situ measurements of post-fire debris flows in southern California: Comparisons of the timing and magnitude of 24 debris-flow events with rainfall and soil moisture conditions. *J. Geophys. Res. Earth Surf.* **2011**, *116*, F4. [CrossRef]
6. Santi, P.M.; Higgins, J.D.; Cannon, S.H.; Gartner, J.E. Sources of debris flow material in burned areas. *Geomorphology* **2008**, *96*, 310–321. [CrossRef]
7. Short, L.E.; Gabet, E.J.; Hoffman, D.F. The role of large woody debris in modulating the dispersal of a post-fire sediment pulse. *Geomorphology* **2015**, *246*, 351–358. [CrossRef]
8. Cheng, D.; Cui, Y.; Su, F.; Jia, Y.; Choi, C.E. The characteristics of the Mocoa compound disaster event, Colombia. *Landslides* **2018**, *15*, 1223–1232. [CrossRef]
9. Ciurleo, M.; Mandaglio, M.C.; Moraci, N. Landslide susceptibility assessment by TRIGRS in a frequently affected shallow instability area. *Landslides* **2018**. [CrossRef]

10. Soeters, R.; van Westen, C.J. Slope instability recognition, analysis and zonation. In *Landslides Investigation and Mitigation*; Turner, A.K., Schuster, R.L., Eds.; TRB Special Report 247; National Academy Press: Washington, DC, USA, 1996; pp. 129–177.
11. Ciurleo, M.; Cascini, L.; Calvello, M. A comparison of statistical and deterministic methods for shallow landslide susceptibility zoning in clayey soils. *Eng. Geol.* **2017**, *223*, 71–81. [CrossRef]
12. Borrelli, L.; Ciurleo, M.; Gulla, G. Shallow landslide susceptibility assessment in granitic rocks using GIS-based statistical methods: The contribution of the weathering grade map. *Landslides* **2018**, *15*, 1127–1142. [CrossRef]
13. Fell, R.; Corominas, J.; Bonnard, C.; Cascini, L.; Leroi, E.; Savage, W.Z. Guidelines for landslide susceptibility, hazard and risk zoning for land use planning. *Eng. Geol.* **2008**, *102*, 85–98. [CrossRef]
14. Cannon, S.H.; Gartner, J.E. *Wildfire-Related Debris Flow from a Hazards Perspective*; Springer: Berlin/Heidelberg, Germany, 2005; pp. 363–385.
15. Cannon, S.H.; Gartner, J.E.; Rupert, M.G.; Michael, J.A.; Djokic, D.; Sreedhar, S. Emergency assessment of debris-flow hazards from basins burned by the grand prix and old fires of 2003. *U.S. Geol. Surv.* **2003**, 45–59. [CrossRef]
16. Gartner, J.E.; Cannon, S.H.; Santi, P.M.; Dewolfe, V.G. Empirical models to predict the volumes of debris flows generated by recently burned basins in the western U.S. *Geomorphology* **2008**, *96*, 339–354. [CrossRef]
17. Cannon, S.H.; Gartner, J.E.; Rupert, M.G.; Michael, J.A.; Rea, A.H.; Parrett, C. Predicting the probability and volume of postwildfire debris flows in the intermountain western united states. *Geol. Soc. Am. Bull.* **2009**, *122*, 127–144. [CrossRef]
18. Gartner, J.E.; Santi, P.M.; Cannon, S.H. Predicting locations of post-fire debris-flow erosion in the san Gabriel mountains of southern California. *Natl. Hazards* **2015**, *77*, 1305–1321. [CrossRef]
19. Friedel, M.J. A data-driven approach for modeling post-fire debris-flow volumes and their uncertainty. *Environ. Model. Softw.* **2011**, *26*, 1583–1598. [CrossRef]
20. Cannon, S.H.; Boldt, E.M.; Laber, J.L.; Kean, J.W.; Staley, D.M. Rainfall intensity–duration thresholds for postfire debris-flow emergency-response planning. *Natl. Hazards* **2011**, *59*, 209–236. [CrossRef]
21. Crosetto, M.; Tarantola, S. Uncertainty and sensitivity analysis: Tools for GIS-based model implementation. *Int. J. Geogr. Inf. Syst.* **2001**, *15*, 415–437. [CrossRef]
22. Xiang, L.; Li, Y.; Chen, H.; Su, F.; Huang, X. Sensitivity analysis of debris flow along highway based on geomorphic evolution theory. *Resour. Environ. Yangtze Basin* **2015**, *24*, 1984–1992.
23. cnBeta.COM. Debris Flow Began to Occur in California after the Mountain Fire Season in the United States. Available online: https://www.cnbeta.com/articles/tech/687749.htm (accessed on 28 May 2018).
24. Schleuss, J.; Smith, D.; Boxall, B. Tracking a Path of Destruction from Montecito's Mountains to the Ocean. Los Angeles Times. Available online: http://www.latimes.com/local/california/la-me-san-ysidro-damage-20180112-htmlstory.html (accessed on 2 April 2018).
25. Hamilton, M.; Serna, J. Montecito Braced for Fire, But Mud Was a More Stealthy, Deadly Threat. Los Angeles Times. Available online: http://www.latimes.com/local/lanow/la-me-montecito-mudslide-main-20180112-story.html (accessed on 2 April 2018).
26. Dolan, J. Search Teams Find 21st Victim of Montecito Mudslide. Los Angeles Times. Available online: http://www.latimes.com/local/lanow/la-me-montecito-death-toll-20180121-story.html (accessed on 26 April 2018).
27. BBC News. California: Thirteen Dead in Montecito Rains and Mudslides. Available online: http://www.bbc.com/news/world-us-canada-42624408 (accessed on 26 April 2018).
28. Robert, D.; Niehaus, I. *The Economic Impacts of the Montecito Mudslides a Preliminary Assessment*; Robert, D., Ed.; Niehaus Inc.; Available online: http://www.rdniehaus.com/rdn/wp-content/uploads/2018/03/RDN_Montecito_Mudslides_Impacts-1.pdf (accessed on 28 May 2018).
29. Magnoli, G. County Estimates $46 Million Cost for Thomas Fire, Montecito Debris Flow Response, Repairs. Available online: https://www.noozhawk.com/article/county_estimates_46m_cost_thomas_fire_montecito_debris_flow_response (accessed on 28 May 2018).
30. U.S. Coast Guard. Santa Barbara County Neighborhood Affected Mudslides—09 Jan 2018. Available online: https://commons.wikimedia.org/wiki/File:Santa_barbara_county_neighborhood_affected_mudslides_-_09_Jan_2018.jpg (accessed on 19 November 2018).

31. Wiley, J. SY Ranch & Casa de Maria Debris Flow 180111-04783. Available online: https://commons.wikimedia.org/wiki/File:SY_Ranch_%26_Casa_de_Maria_Debris_Flow_180111-04783.jpg (accessed on 19 November 2018).
32. Roy, D.P.; Wulder, M.A.; Loveland, T.R.; Woodcock, C.E.; Allen, R.G.; Anderson, M.C.; Helder, D.; Irons, J.R.; Johnson, D.M.; Kennedy, R. Landsat-8: Science and product vision for terrestrial global change research. *Remote Sens. Environ.* **2014**, *145*, 154–172. [CrossRef]
33. Arvidson, T.; Gasch, J.; Goward, S.N. Landsat 7's long-term acquisition plan—An innovative approach to building a global imagery archive. *Remote Sens. Environ.* **2001**, *78*, 13–26. [CrossRef]
34. Fernández-Manso, A.; Fernández-Manso, O.; Quintano, C. Sentinel-2A red-edge spectral indices suitability for discriminating burn severity. *Int. J. Appl. Earth Obs. Geoinf.* **2016**, *50*, 170–175. [CrossRef]
35. Harald, V.D.W.; Freek, V.D.M. Sentinel-2A MSI and Landsat 8 OLI provide data continuity for geological remote sensing. *Remote Sens.* **2016**, *8*, 883.
36. Gao, K.; Cui, P.; Zhao, C.; Wei, F. Landslide hazard evaluation of Wanzhou based on GIS information value method in the three gorges reservoir. *Chin. J. Rock Mech. Eng.* **2006**, *25*, 991–996.
37. Chen, X.Q.; Cui, P.; Yang, Z.; Qi, Y.Q. Change in glaciers and glacier lakes in Boiqu River basin, middle Himalayas during last 15 years. *J. Glaciol. Geocryol.* **2005**, *27*, 793–800.
38. World Weather Online. Santa Barbara Historical Weather. Available online: https://www.worldweatheronline.com/santa-barbara-weather-history/california/us.aspx (accessed on 28 May 2018).
39. Monitoring Forest Fire Points Using SWIR and LWIR Band of Landsat 8 Data. Available online: http://blog.sina.com.cn/s/blog_764b1e9d0102vnxr.html (accessed on 27 April 2018).
40. Jiang, S.; Gong, C.L.; Yong, H.U.; Meng, P. Comparison of radiation characteristics of forest fire and background in short wave infrared absorption bands. *J. Atmos. Environ. Opt.* **2014**, *9*, 223–228.
41. Veraverbeke, S.; Verstraeten, W.W.; Lhermitte, S.; Goossens, R. Evaluating landsat thematic mapper spectral indices for estimating burn severity of the 2007 Peloponnese wildfires in Greece. *Int. J. Wildland Fire* **2010**, *19*, 558–569. [CrossRef]
42. Lentile, L.B.; Holden, Z.A.; Smith, A.M.; Falkowski, M.J.; Hudak, A.T.; Morgan, P.; Lewis, S.A.; Gessler, P.E.; Benson, N.C. Remote sensing techniques to assess active fire characteristics and post-fire effects. *Int. J. Wildland Fire* **2006**, *15*, 319–345. [CrossRef]
43. Norton, J.M. The Use of Remote Sensing Indices to Determine Wildland Burn Severity in Semiarid Sagebrush Steppe Rangelands Using Landsat ETM+ and SPOT 5. Available online: http://giscenter.isu.edu/research/techpg/nasa_tlcc/PDF/Ch6.pdf (accessed on 30 October 2018).
44. Karl, J. Normalized Burn Ratio. Available online: http://wiki.landscapetoolbox.org/doku.php/remote_sensing_methods:normalized_burn_ratio (accessed on 30 October 2018).
45. Zou, Q.; Cui, P.; Zeng, C.; Tang, J.; Regmi, A.D. Dynamic process-based risk assessment of debris flow on a local scale. *Phys. Geogr.* **2016**, *37*, 132–152. [CrossRef]
46. Chen, X.; Cui, P.; You, Y.; Liu, J. Post-earthquake changes and prediction of debris flow scales in Subao river valley, Beichuan county, Sichuan province, China. *Environ. Earth Sci.* **2012**, *65*, 995–1003. [CrossRef]
47. Choi, C.; Cui, Y.; Au, K.; Liu, H.; Wang, J.; Liu, D.; Wang, H. Case study: Effects of a partial-debris dam on riverbank erosion in the Parlung Tsangpo river, China. *Water* **2018**, *10*, 250. [CrossRef]
48. Jenson, S.K.; Domingue, J.O. Extracting topographic structure from digital elevation data for geographic information-system analysis. *Photogramm. Eng. Remote Sens.* **1988**, *54*, 1593–1600.
49. O'Callaghan, J.F.; Mark, D.M. The extraction of drainage networks from digital elevation data. *Comput. Vis. Graph. Image Process.* **1984**, *28*, 323–344. [CrossRef]
50. Strahler, A.N. Hypsometric (area-altitude) analysis of erosional topography. *Geol. Soc. Am. Bull.* **1952**, *63*, 1117–1142. [CrossRef]
51. Pike, R.J.; Wilson, S.E. Elevation-relief ratio, hypsometric integral, and geomorphic area-altitude analysis. *Geol. Soc. Am. Bull.* **1971**, *82*, 1079–1083. [CrossRef]
52. Chang, Z.; Wang, J.; Bai, S.; Zhang, Z. Comparison of hypsometric integral methods. *J. Arid Land Resour. Environ.* **2015**, *29*, 171–175.
53. Yesilnacar, E.; Topal, T. Landslide susceptibility mapping: A comparison of logistic regression and neural networks methods in a medium scale study, Hendek region (Turkey). *Eng. Geol.* **2005**, *79*, 251–266. [CrossRef]

54. Yilmaz, I. Comparison of landslide susceptibility mapping methodologies for Koyulhisar, Turkey: Conditional probability, logistic regression, artificial neural networks, and support vector machine. *Environ. Earth Sci.* **2010**, *61*, 821–836. [CrossRef]
55. Trigila, A.; Frattini, P.; Casagli, N.; Catani, F.; Crosta, G.; Esposito, C.; Lagomarsino, D.; Mugnozza, G.S.; Segoni, S.; Spizzichino, D.; et al. Landslide susceptibility mapping at national scale: The Italian case study. In *Landslide Science and Practice*; Springer: Berlin/Heidelberg, Germany, 2013; pp. 287–295.
56. Lee, S. Application of logistic regression model and its validation for landslide susceptibility mapping using GIS and remote sensing data. *Int. J. Remote Sens.* **2005**, *26*, 1477–1491. [CrossRef]
57. Lee, S.; Ryu, J.H.; Kim, I.S. Landslide susceptibility analysis and its verification using likelihood ratio, logistic regression, and artificial neural network models: Case study of Youngin, Korea. *Landslides* **2007**, *4*, 327–338. [CrossRef]
58. Manzo, G.; Tofani, V.; Segoni, S.; Battistini, A.; Catani, F. GIS techniques for regional-scale landslide susceptibility assessment: The Sicily (Italy) case study. *Int. J. Geogr. Inf. Sci.* **2013**, *27*, 1433–1452. [CrossRef]
59. Van Den Eeckhaut, M.; Hervás, J.; Jaedicke, C.; Malet, J.P.; Montanarella, L.; Nadim, F. Statistical modelling of Europe-wide landslide susceptibility using limited landslide inventory data. *Landslides* **2012**, *9*, 357–369. [CrossRef]
60. Seal, H.L. Estimation of the probability of an event as a function of several independent variables. *Biometrika* **1967**, *54*, 167–179.
61. Xu, C.; Xu, X.W. Logistic regression model and its validation for hazard mapping of landslides triggered by Yushu earthquake. *J. Eng. Geol.* **2012**, *20*, 326–333.
62. USGS. Global Data Explore. Available online: https://gdex.cr.usgs.gov/gdex/ (accessed on 28 May 2018).
63. Singh, O.; Sarangi, A.; Sharma, M.C. Hypsometric integral estimation methods and its relevance on erosion status of north-western lesser Himalayan watersheds. *Water Resour. Manag.* **2008**, *22*, 1545–1560. [CrossRef]
64. USGS. Post-Fire Flooding and Debris Flow. Available online: https://ca.water.usgs.gov/wildfires/wildfires-debris-flow.html (accessed on 21 June 2018).
65. Bui, D.T.; Nguyen, Q.P.; Hoang, N.D.; Klempe, H. A novel fuzzy K-nearest neighbor inference model with differential evolution for spatial prediction of rainfall-induced shallow landslides in a tropical hilly area using GIS. *Landslides* **2017**, *14*, 1–17.
66. Fressard, M.; Thiery, Y.; Maquaire, O. Which data for quantitative landslide susceptibility mapping at operational scale? Case study of the Pays d'Auge plateau hillslopes (Normandy, France). *Natl. Hazards Earth Syst. Sci.* **2014**, *14*, 569–588. [CrossRef]